Mon. Not. R. Astron. Soc. **000**, 000–000 (2003)

Gravitational lens magnification by Abell 1689: Distortion of the background galaxy luminosity function

S. Dye[1], A.N. Taylor[1], E.M. Thommes[1,2], K. Meisenheimer[2], C. Wolf[2], J.A. Peacock[1]
[1] *Institute for Astronomy, University of Edinburgh, Royal Observatory, Blackford Hill, Edinburgh EH9 3HJ, U.K.*
[2] *Max-Planck-Institut für Astronomie, Königstuhl 17, D-69117 Heidelberg, Germany*

8 January 2003

ABSTRACT
Gravitational lensing magnifies the observed flux of galaxies behind the lens. We use this effect to constrain the total mass in the cluster Abell 1689 by comparing the lensed luminosities of background galaxies with the luminosity function of an undistorted field. Under the assumption that these galaxies are a random sample of luminosity space, this method is not limited by clustering noise. We use photometric redshift information to estimate galaxy distance and intrinsic luminosity. Knowing the redshift distribution of the background population allows us to lift the mass/background degeneracy common to lensing analysis. In this paper we use 9 filters observed over 12 hours with the Calar Alto 3.5m telescope to determine the redshifts of 1000 galaxies in the field of Abell 1689. Using a complete sample of 146 background galaxies we measure the cluster mass profile. We find that the total projected mass interior to $0.25\,h^{-1}\,\mathrm{Mpc}$ is $M_{2d}(< 0.25\,h^{-1}\,\mathrm{Mpc}) = (0.48 \pm 0.16) \times 10^{15}\,h^{-1}\mathrm{M}_{\odot}$, where our error budget includes uncertainties from the photometric redshift determination, the uncertainty in the offset calibration and finite sampling. This result is in good agreement with that found by number count and shear–based methods and provides a new and independent method to determine cluster masses.

Key words: galaxies: clusters: general - cosmology: theory - gravitational lensing - large scale structure of Universe.

1 INTRODUCTION

The use of gravitational lensing as a means of cluster mass reconstruction provides a theoretically efficient approach without the equilibrium and symmetry assumptions which typically accompany virial and X-ray temperature methods. Mass determination through application of lens shear proves to give good resolution in mass maps although measurement of absolute quantities is not possible without external calibration. This so called sheet-mass degeneracy (Falco, Gorenstein & Shapiro 1985) is broken however by methods which exploit the property of lens magnification.

First recognised by Broadhurst, Taylor & Peacock (1995, BTP hereafter) as a viable tool for the reconstruction of cluster mass, lens magnification has the twofold effect of amplifying background source galaxy fluxes as well as their geometrical size and separation. This immediately permits two separate approaches for measuring lensing mass. The first involves selecting a sample of sources with a flat or near-flat number count slope. Magnification results in a reduction of their local surface number density owing to the dominance of their increased separation over the enhanced number detectable due to flux amplification.

Although contaminated by faint cluster members, Fort, Mellier & Dantel-Fort (1997) first reported this dilution effect using B and I band observations of the cluster CL0024+1654. Later, Taylor et al. (1998, T98 hereafter) demonstrated how the dilution in surface number density of a colour-selected sample of red galaxies lying behind the cluster Abell 1689 enables determination of its total mass profile and 2d distribution. A projected mass interior to $0.24\,h^{-1}\,\mathrm{Mpc}$ of $M_{2d}(< 0.24\,h^{-1}\,\mathrm{Mpc}) = (0.50 \pm 0.09) \times 10^{15}\,h^{-1}\mathrm{M}_{\odot}$ was predicted, in good agreement with the shear analysis of Tyson & Fischer (1995) who measured $M_{2d}(< 0.24\,h^{-1}\,\mathrm{Mpc}) = (0.43 \pm 0.02) \times 10^{15}\,h^{-1}\mathrm{M}_{\odot}$ and Kaiser (1995) with a measurement of $M_{2d}(< 0.24\,h^{-1}\,\mathrm{Mpc}) = (0.43 \pm 0.04) \times 10^{15}\,h^{-1}\mathrm{M}_{\odot}$.

Since then, several authors have detected source number count depletion due to cluster lensing. Athreya et al (1999) observe MS1008−1224 and use photometric redshifts to identify a background population of galaxies within which they measure depletion. Mayen & Soucail (2000) constrain the mass profile of MS1008−1224 by comparing to simulations of depletion curves. Gray et al (2000) measure the first depletion in the near infra-red due to lensing by Abell 2219. Finally and most recently, Rögnvaldsson et al. (2000) find

depletion in the source counts behind CL0024+1654 in the R band and for the first time, in the U band.

The second mass reconstruction approach permitted by magnification forms the primary focus of this paper. The amplification of flux by lens magnification introduces a measurable shift in the luminosity function of background source galaxies. With a sufficiently well defined luminosity function derived from an unlensed offset field for comparison, this shift can be measured to allow an estimate of the lens mass (BTP). This method relies upon a set of observed source magnitudes which, if assumed to form an effective random sampling of luminosity space, is not limited by noise from background source clustering unlike the number count method (see Section 5.2 for further discussion).

This paper presents the first application of mass reconstruction using lens flux magnification inferred from the luminosity function of background samples. Unlike the method of T98 who defined their background sample based on colour cuts, in this work photometric redshifts of all objects in the observed field have been estimated. This not only allows an unambiguous background source selection but alleviates the need to estimate source distances when scaling convergence to real lens mass.

The following section details the theory of mass reconstruction from lens magnification of background source magnitudes. Section 3 describes the photometric analysis applied to observations of A1689 with the redshifts which result. Observations of the offset field which provide the absolute magnitude distribution required for comparison with the A1689 background source sample are presented in Section 4. From this, a parameterised luminosity function is calculated in Section 4.2 necessary for application of the maximum likelihood method. Following a discussion of sample incompleteness in Section 5.1, a mass measurement of A1689 is given in Section 6 where the effects of sample incompleteness are quantified. Finally, a signal to noise study is carried out in Section 7 to investigate the effects of shot noise, calibration uncertainty of the offset field and photometric redshift error.

2 MASS RECONSTRUCTION

Measurement of lens magnification of background source fluxes requires a statistical approach in much the same way as do shear or number count depletion studies. The basis of this statistical method relies on the comparison of the distribution of lensed source luminosities with the luminosity function of an un-lensed offset field. As Section 5.2 discusses further, for a fair comparison, the population of sources detected behind the lens must be consistent with the population of objects used to form this un-lensed reference luminosity function.

The effect of lens magnification by a factor μ on a source is to translate its observed magnitude from M to $M + 2.5\log_{10}\mu$. In terms of the reference luminosity function, $\phi(M,z)$, the probability of a background galaxy with an absolute magnitude M and redshift z being magnified by a factor μ is (BTP)

$$\mathrm{P}[M|\mu,z] = \frac{\phi(M + 2.5\log_{10}\mu(z),z)}{\int \phi(M + 2.5\log_{10}\mu(z),z)\mathrm{d}M}. \quad (1)$$

Magnification depends on the geometry of the observer-lens-source system hence for a fixed lens and observer, μ is a function of source redshift. This redshift dependence comes from the familiar dimensionless lens surface mass density or convergence, $\kappa(z)$, and shear, $\gamma(z)$, which are related to $\mu(z)$ via,

$$\mu(z) = \left|[1-\kappa(z)]^2 - \gamma^2(z)\right|^{-1}. \quad (2)$$

We wish to apply maximum likelihood theory using the probability in equation (1) to determine lens magnification and hence κ. A parametric luminosity function is therefore required and so we take $\phi(M,z)$ to be a Schechter function (Schechter 1976),

$$\phi(M,z) = \phi^*(z)10^{0.4(M_*-M)(1+\alpha)}\exp\left[-10^{0.4(M_*-M)}\right]. \quad (3)$$

The Schechter parameters ϕ^*, M_* and α are determined by fitting to the magnitude distribution of the offset field (see Section 4). T98 use μ as a likelihood parameter by adopting the simplification that all sources lie at the same redshift. However this is not possible when each source is attributed its own redshift. We must therefore express μ in terms of a redshift depenent quantity and a source–independent likelihood parameter.

The most direct solution is to separate the convergence. Using the parameter κ_∞ introduced by BTP as the convergence for sources at $z=\infty$, we can write $\kappa(z)$ as,

$$\begin{aligned}\kappa(z) &= \kappa_\infty f(z),\\ f(z) &= \frac{\sqrt{1+z}-\sqrt{1+z_L}}{\sqrt{1+z}-1}.\end{aligned} \quad (4)$$

We therefore choose κ_∞ as our likelihood parameter with all source redshift dependency being absorbed into the function f. The lens surface mass density, Σ, is then related to κ_∞ and the lens redshift, z_L, by

$$\begin{aligned}\Sigma(z_L) &= \frac{cH_0}{8\pi G}\kappa_\infty\left[\frac{(1+z_L)^2}{\sqrt{1+z_L}-1}\right]\\ &= 2.75\times10^{14}\kappa_\infty\left[\frac{(1+z_L)^2}{\sqrt{1+z_L}-1}\right]hM_\odot\mathrm{Mpc}^{-2}.\end{aligned} \quad (5)$$

Here, we assume an Einstein-de-Sitter universe for reasons of simplicity and because BTP show that this result depends only weakly on the chosen cosmological model.

Before choosing a likelihood function, consideration must be given to the shear term in equation (2). Since shear scales with source redshift in the same way as the convergence, we use the so-called κ estimators discussed by T98 which relate κ to γ. At the extremes these are $\gamma=\kappa$ for the isothermal sphere or $\gamma=0$ for the sheet-like mass. A third variation, motivated by cluster simulations and the fact that it has an invertible $\mu(\kappa)$ relation, is $\gamma\propto\kappa^{1/2}$ (van Kampen 1998). This gives rise to the parabolic estimator which predicts values of κ between those given by the sheet and isothermal estimators. Using equation (2), the magnification for these three different cases therefore relates to κ_∞ via

$$\mu(z) = \begin{cases} |1-2\kappa_\infty f(z)|^{-1} & \text{iso.}\\ |[\kappa_\infty f(z)-c]\,[\kappa_\infty f(z)-1/c]|^{-1} & \text{para.}\\ [1-\kappa_\infty f(z)]^{-2} & \text{sheet}\end{cases} \quad (6)$$

and hence three different estimations of κ_∞ exist for a given μ. The constant c in the parabolic case is chosen to provide

the best fit with the cluster simulations. As in T98, we take $c = 0.7$ throughout this paper.

The likelihood function for κ_∞ is then formed from equation (1),

$$\mathcal{L}(\kappa_\infty) \propto \prod_i \mathrm{P}[M_i|\mu(\kappa_\infty), z_i] \tag{7}$$

where μ is one of the three forms in equation (6) and the product applies to the galaxies behind the cluster region under scrutiny. Absolute surface mass densities are then calculated from κ_∞ using equation (5).

The probability distribution for κ_∞ obtained from equation (1) for a single galaxy is typically double-peaked as two solutions for κ_∞ exist for a given magnification. The choice of peak is determined by image parity such that the peak at the higher value of κ_∞ is chosen for a galaxy lying inside the critical line and vice versa. The chosen peak is then extrapolated to extend over the full κ_∞ range before contributing to the likelihood distribution. In this way, a single-peaked likelihood distribution is obtained.

Evidently, calculation of lens surface mass density in this way requires redshift and absolute magnitude data for background galaxies together with knowledge of the intrinsic distribution of magnitudes from an unlensed offset field. The next section details the photometric analysis applied to our observations of Abell 1689 to arrive at background object redshifts and absolute magnitudes.

3 PHOTOMETRIC ANALYSIS

3.1 Data acquisition

Observations of Abell 1689 were performed with the Calar Alto 3.5m telescope in Spain using 8 different filters, chosen for photometric distinction between foreground, cluster and background objects. In addition, the I-band observations of T98 were included to bring the combined exposure time to a total of exactly 12 hours worth of useable data characterised by a seeing better than $2.1''$. Table 1 details the summed integration time for each filter set together with the motivation for inclusion of the filter. Note the narrow band filters 466/8, 480/10 and 774/13 which were selected to pick out spectral features of objects lying at the cluster redshift of $z = 0.185$ (Teague, Carter & Gray 1990).

Image reduction and photometry was performed using the MPIAPHOT (Meisenheimer & Röser 1996) software written at the MPIA Heidelberg as an extension to the MIDAS reduction software package. Images were de-biased and flattened from typically four or five median filtered dusk sky flats observed each night for each filter set. Any large scale remnant flux gradients were subsequently removed by flattening with a second-order polynomial fitted to the image background. Cosmic ray removal was carried out using the pixel rejection algorithm incorporated in MPIAPHOT. All post-reduced images were flattened to a 1σ background flux variation of less than 0.02 mag.

3.2 Galaxy catalogue

Instead of co-adding images in each filter set before object detection, photometric evaluation was carried out on images individually. In this way, an estimate of the uncertainty in the photon count for each galaxy could be obtained. The mean photon count $I^{(b,m)}$ of a galaxy m observed in a filter b was calculated as the usual reciprocal-variance weighted sum,

$$I^{(b,m)} = \sum_i \frac{I_i^{(b,m)}}{\left(\sigma_i^{(b,m)}\right)^2} \Big/ \left[\sum_i \left(\sigma_i^{(b,m)}\right)^{-2}\right] \tag{8}$$

where the summation acts over all images belonging to a particular filter set and the error on $I^{(b,m)}$ is

$$\overline{\sigma}^{(b,m)} = \left[\sum_i \left(\sigma_i^{(b,m)}\right)^{-2}\right]^{-1/2}. \tag{9}$$

The quantity $\sigma_i^{(b,m)}$ is the standard deviation of background pixel values surrounding galaxy m in image i. Background pixels were segregated by applying an appropriate cut to the histogram of counts in pixels within a box of size $13'' \times 13''$ (40×40 pixels) centred on the galaxy. This cut removed the high count pixels belonging to the galaxy itself and any other neighbouring galaxies within the box.

Integrated galaxy photon counts were determined using MPIAPHOT which sums together counts in all pixels lying inside a fixed aperture of radius $6''$ centred on each galaxy. A 'mark table' accompanying every image in every filter-set provided co-ordinates of galaxy centres. Tables were fit within an accuracy of $< 1''$ to individual images using copies of a master table derived from the deepest co-added image; that observed in the I-band. In this way consistent indexing of each galaxy was achieved throughout all catalogues. The master table was generated using the object detection software 'SExtractor' (Bertin & Arnouts 1996). Only galaxies were contained in the master table, star-like objects being removed after identification by their high brightness and low FWHM. With a detection threshold of 3σ above the average background flux, galaxies in the I-band image were catalogued after coincidence matching with objects detected at the 3σ level in the associated V-band data presented by T98. Despite cataloguing ~ 3000 galaxies, the resulting number was limited to a total of ~ 1000 due to the relatively shallow data observed with the 466/8 narrow-band filter.

Filter: $\lambda_c/\Delta\lambda$ (nm)	t_{int}(s)	Use
826/137 (I-band)	6000	Global SED
774/13	6800	H_α at $z = 0.185$
703/34	4100	Background z
614/28	7700	Background z
572/21	6300	Background z
530/35	3300	Background z
480/10	4200	4000Åat $z = 0.185$
466/8	4800	Ca H,K at $z = 0.185$
457/96 (B-band)	6000	Global SED

Table 1. The observations of Abell 1689 in all 9 filters (labelled as $\lambda_c/\Delta\lambda \equiv$ central wavelength/FWHM). t_{int} gives the total integration time in each filter. The I-band data comes from T98.

3.3 Photometry

The integration of photon counts in an aperture of fixed size requires constant seeing across all images to allow correct determination of colours. To ensure constant seeing, all images were degraded by Gaussian convolution to the worst seeing of $2.1''$ measured in the 466/8 filter before galaxy counts were evaluated. The effects of changing weather conditions were compensated for by normalising images within each filter set to an arbitrarily chosen image in that set. Normalisation was conducted by scaling the galaxy counts in each image so that the average counts of the same stars in all images was equal. This ensured correct calculation of the weighted counts and the error from equation (8) and (9). These quantities were later scaled to their calibrated photometric values.

Calibration of the photometric fluxes from the weighted counts was provided using the spectrum of the dominant elliptical galaxy in the centre of A1689 taken from Pickles & van der Kruit (1991). Denoting this spectrum as the function $F_s(\lambda)$, the calibration scale factors k_b for each filter b were calculated using

$$I^{(b,s)} = k_b \int \mathrm{d}\lambda \frac{E(\lambda)T_b(\lambda)F_s(\lambda)\lambda}{hc} \tag{10}$$

where the function $T_b(\lambda)$ describes the filter transmission efficiency, $E(\lambda)$ is the combined filter-independent efficiency of the detector and telescope optics and $I^{(b,s)}$ is the measured integrated photon count rate of the central galaxy. The values of k_b obtained in this way were only relatively correct owing to the lack of an absolute calibration of the published spectrum. Absolute calibration scale factors were calculated from observations of the standard star G60-54 (Oke 1990) in all filters in exactly the same manner. Verification of this absolute calibration was provided by the consistency of ratios of k_b(absolute)/k_b(relative) to a zero point of $\Delta m = 2.11 \pm 0.01$ magnitudes averaged over all filters.

Consideration of equation (10) shows that only the quantity

$$\int \mathrm{d}\lambda E(\lambda)T_b(\lambda)F_m(\lambda)\lambda = \frac{hc\, I^{(b,m)}}{k_b} \tag{11}$$

can be known for any galaxy m with a calibrated photon count rate. The required photometric flux

$$F^{(b,m)} = \int \mathrm{d}\lambda T_b(\lambda)F_m(\lambda) \tag{12}$$

can not therefore be directly determined without making an approximation such as the simplification of filter transmission curves to top hat functions. Although this is acceptably accurate in narrow band filters, it is not for broad band filters. This problem was avoided by the more sophisticated technique of fitting model spectra to measured galaxy colours as the next section discusses.

3.4 Photometric redshift evaluation

Direct calculation of photometric fluxes using equation (12) was made possible by fitting model spectra to the set of calibrated photon count rates measured for each galaxy across all filters. Expressed more quantitatively, equation (11) was applied for each filter to a library of template spectra to arrive at a set of scaled filter counts for each spectrum. Galaxies were then allocated library spectra by finding the set of library colours which best fit the measured galaxy colours. Note that this differs from conventional template fitting where spectra are redshifted and scaled to fit observed colours in a much more time costly manner.

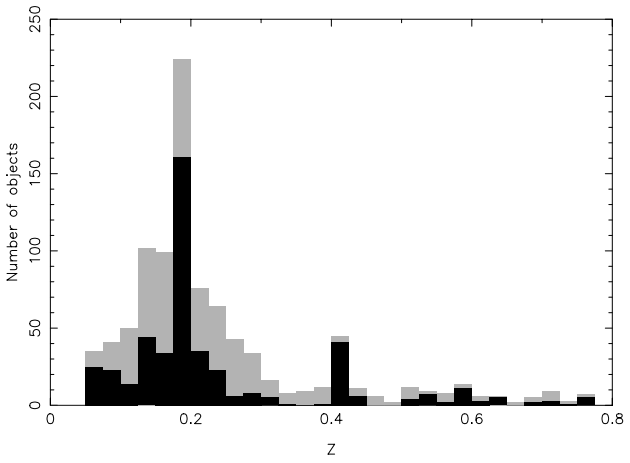

Figure 1. Redshift distribution of the 958 objects photometrically evaluated in the field of A1689. The grey histogram plots all 958 redshifts whereas the black histogram plots only the 470 redshifts with a 1σ error in redshift of less than 0.05. The peak at $z \simeq 0.18$ is the contribution from the cluster galaxies.

The spectral library was formed from the template galaxy spectra of Kinney et al. (1996). A regular grid of galaxy templates was generated, varying in redshift along one axis from $z = 0$ to $z = 1.6$ in steps of $\Delta z = 0.002$ and ranging over 100 spectral types from ellipticals, through spirals to starbursts along the other.

The set of photometric errors given by equation (9) for an individual galaxy across all filters gives rise to an error ellipsoid in colour space. Using the size and location of these error ellipsoids, probabilities of each library entry causing the observed sets of colours for each galaxy were then calculated as

$$p(\boldsymbol{q}|z,s) = \frac{1}{\sqrt{(2\pi)^n |V|}} \exp\left(-\frac{1}{2}\sum_{j=1}^{n} \frac{[q_j - Q_j(z,s)]^2}{\sigma_j^2}\right) \tag{13}$$

where n is the number of colours, σ_j comes from propagation of the error given by equation (9) and $V \equiv \mathrm{diag}(\sigma_1^2, ..., \sigma_n^2)$. Each galaxy's position vector in colour space, $\boldsymbol{q} \equiv (q_1, ..., q_n)$ is compared with the colour vector $\boldsymbol{Q}$ of the library spectrum with a given redshift z and type s. Finding the maximum probability corresponding to the closest set of matching colours therefore immediately establishes redshift and galaxy type. An assessment of the uncertainty in this redshift is subsequently obtained directly from the distribution of the probabilities associated with neighbouring library spectra.

Figure 1 shows the distribution of the 958 successfully classified galaxy redshifts estimated from the full filter set. We measure an average redshift error of $\langle \sigma_z \rangle = 0.08$. The

maximum redshift limit of $z \simeq 0.8$ comes from the condition that the 4000Å limit must lie in or blue-ward of the second reddest filter in the set. The peak at $z \simeq 0.18$ in Figure 1 is clearly the contribution from the cluster galaxies.

The feature at $z \simeq 0.4$ is most likely real and not an artifact of the photometric method. Such artifacts occur due to 'redshift focusing' when particular redshifts are measured more accurately than others. Where the uncertainty is larger, galaxies can be randomly scattered out of redshift bins, producing under-densities and corresponding over-densities where the redshift measurement is more accurate. This effect depends on the details of the filter set, being more common when fewer filters are used, but can be modelled by Monte Carlo methods.

The top half of Figure 2 shows the results of one realisation of such a Monte Carlo test for redshift focusing. The plot indicates how accurately the method reproduces redshifts of spectra scaled to I = 20 with photometric noise levels taken from the A1689 filter set. Each point represents a single library spectrum. Reproduced spectral redshifts, $z_{\rm phot}$, were determined by calculating colours through application of equation (12) to the library spectra with redshifts $z_{\rm lib}$. These colours were then randomly scattered by an amount determined from the filter-specific photometric error measured in the A1689 data before application of the redshift estimation method outlined above. The bottom half of Figure 2 shows the same plot generated using spectra scaled to I = 21 with the same photometric error taken from the A1689 data.

The accuracy of reproduced redshifts at I = 20 is clearly better than those at I = 21 where photometric noise is more dominant. The lack of any sign of redshift focusing in the vicinity of $z \simeq 0.4$ leads us to conclude that the feature seen at this redshift in the A1689 data is probably real. The I = 21 plot which corresponds approximately to our sample magnitude cut of B = 23.6 (see Section 5.1) shows that galaxies at redshifs below $z = 0.05$ have on average higher estimated redshifts. This only marginally affects the overall redshift distribution and yet partly explains the lack of galaxies at $z < 0.05$ in the A1689 redshifts of Figure 1. It is worth emphasising here that the significance of the peak at $z \simeq 0.18$ attributed to the cluster galaxies is far in excess of any effects of redshift focusing.

Figure 3 shows a comparison of the photometrically determined redshifts $z_{\rm phot}$ around the peak of the redshift distribution of Abell 1689, with spectroscopically determined (Teague, Carter & Gray, 1990) redshifts $z_{\rm spec}$. A very slight bias between $z_{\rm phot}$ and $z_{\rm spec}$ can be seen. This bias is quantified by fitting the line $z_{\rm phot} = z_{\rm spec} + c$ by least-squares to the data points which gives $c = 0.0036$. Referring to equation (28) shows that if this small bias is applied to all redshifts in our sample, a negligible difference of $\Delta\kappa_\infty = 0.001$ would result. Our filter set was selected primarily to distinguish the cluster members, hence at higher redshift we must rely on our Monte Carlo estimates of the redshift uncertainty (see Section 6.1).

Abell 1689 lies in a region of sky where there is a very low level of galactic dust. Our redshifts are therefore not affected by this source of contamination. However, dust in the cluster itself is another concern. We have modelled the effects of reddening by cluster dust and find that although

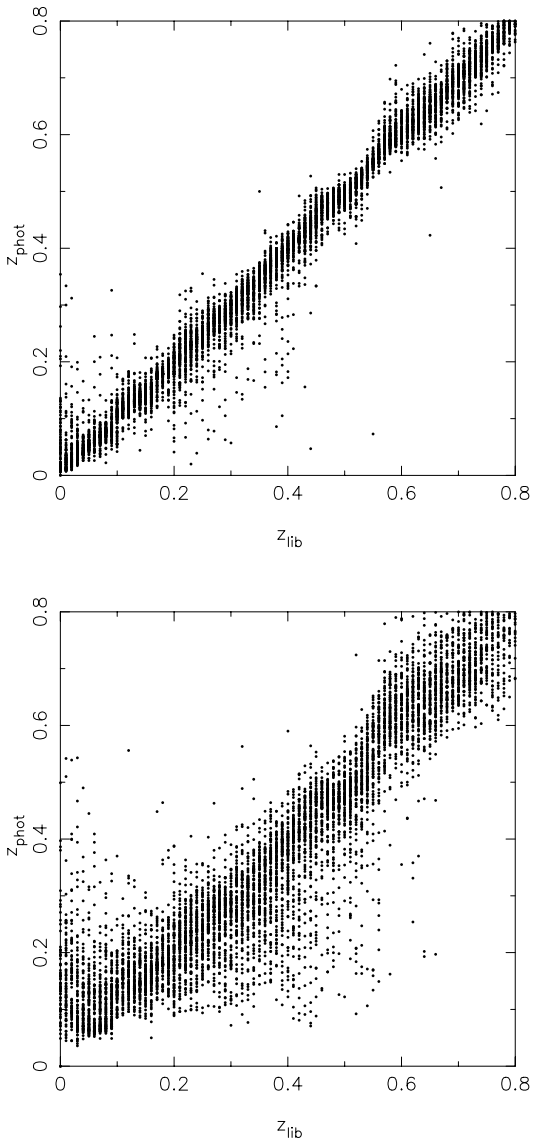

Figure 2. A single Monte Carlo realisation showing the accuracy of the photometric redshift evaluation method. Input library spectra with redshifts $z_{\rm lib}$ are scaled to I = 20 (top) and I = 21 (bottom) and subsequently used to calculate sets of colours using the A1689 filterset. These colours are randomly scattered by the filter-specific photometric errors measured in the A1689 data before calculating the reproduced redshifts $z_{\rm phot}$.

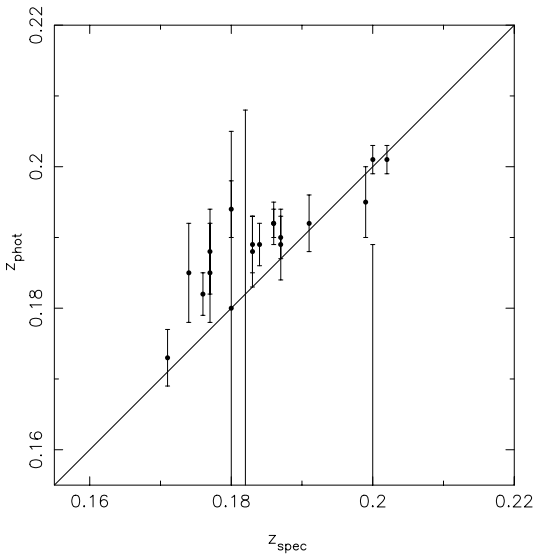

Figure 3. Comparison of the photometric redshifts estimated in the cluster Abell 1689 with spectroscopically determined redshifts. The distribution shows slight non-Gaussianity in the error distribution. The mean redshift of the cluster determined spectroscopically is $z = 0.185$ (Teague, Carter & Gray 1990), while the mean photometric redshift is $z = 0.189 \pm 0.005$.

magnitudes are slightly affected, the redshifts remain the same.

4 OFFSET FIELD AND LENS CALIBRATION

The unlensed, intrinsic magnitude distribution required by the likelihood analysis was taken from an offset field observed as part of the Calar Alto Deep Imaging Survey (CADIS) conducted by the Max-Planck Institut für Astronomie, Heidelberg (Meisenheimer et al. 1998). Data for this survey were observed to a complete depth of B $\simeq$ 24.5 mag in 16 filters from the B-band to the K-band with the 2.2m telescope at Calar Alto. We use the CADIS 16-hour field for our mass calibration.

Using exactly the same methods outlined in the previous section for the A1689 data, photometric redshifts and rest-frame absolute magnitudes were determined for all objects in the field. In addition to galaxy templates in the spectral library however, quasar spectra from Francis et al. (1991) and stellar spectra from Gunn & Stryker (1983) were also included, the primary motivation for this difference being the CADIS quasar study. As a by-product, a more sophisticated object classification method was achieved by finding the overall object class yielding the highest significant probability given by equation (13). Details of this and the CADIS quasar study are given in Wolf et al. (1999). To ensure a fair comparison between the offset field and the cluster field, the CADIS B-band ($\lambda_c/\Delta\lambda = 461/113$ nm) galaxy magnitudes were used with the A1689 B-band magnitudes in the likelihood analysis discussed in Section 2.

Investigation of evolution (see for example, Lilly et al. 1995, Ellis et al. 1996) of the CADIS luminosity function is left for future work. A preliminary study indicated no significant evolution which would impact on the lens mass determination. We therefore applied the same redshift selection as used for the Abell 1689 background sources, and assumed a no–evolution model.

We present two estimates of the calibration B-band luminosity function: a nonparametric $1/V_{\rm max}$ method (Section 4.1) and a maximum likelihood parametric fit to a Schechter function (Section 4.2). The former method allows us to see the distribution of luminosities without imposing a preconceived function, and gives a visual impression of the uncertainties in the parametric fit. In addition the $V_{\rm max}$ approach allows us to make basic tests for sample completeness (we discuss this in Section 5.1). The latter maximum likelihood fit provides a convenient function for performing the second likelihood analysis to determine lens magnification. We begin by describing the nonparametric method.

4.1 The nonparametric CADIS B-band luminosity function

An estimate of the luminosity function of galaxies in the CADIS B band was provided initially using the canonical $1/V_{\rm max}$ method of Schmidt (1968). The quantity $V_{\rm max}$ is computed for each galaxy as the comoving volume within which the galaxy could lie and still remain in the redshift and magnitude limits of the survey. For an Einstein-de-Sitter universe, this volume is,

$$V_{\rm max} = \left(\frac{c}{H_0}\right)^3 \delta\omega \int_{\max(z_l, z_{m_{\rm min}})}^{\min(z_u, z_{m_{\rm max}})} {\rm d}z \frac{D^2(z)}{(1+z)^{3/2}} \qquad (14)$$

where $\delta\omega$ is the solid angle of the observed field of view and $D(z)$ is

$$D(z) = 2(1 - (1+z)^{-1/2}). \qquad (15)$$

The upper limit of the integral in equation (14) is set by the minimum of the upper limit of the redshift interval chosen, z_u, and the redshift at which the galaxy would have to lie to have an apparent magnitude of the faint limit of the survey, $z_{m_{\rm max}}$. Similarly, the maximum of the lower limit of the chosen redshift interval, z_l, and the redshift at which the galaxy would have to lie to have an apparent magnitude of the bright limit of the survey, $z_{m_{\rm min}}$, forms the lower limit of the integral. This lower integral limit plays a non-crucial role when integrating over large volumes originating close to the observer where the volume element makes only a relatively small contribution to $V_{\rm max}$.

The redshifts $z_{m_{\rm max}}$ and $z_{m_{\rm min}}$ are calculated for each object by finding the roots of

$$M - m_{\rm lim} + 5\log_{10}\left[\frac{(1+z)D(z)}{h_0}\right] - K(z) = -42.39 \qquad (16)$$

where M is the absolute magnitude of the object, $m_{\rm lim}$ is the appropriate maximum or minimum survey limit and $K(z)$ is the K-correction. Although the K-correction for each object at its actual redshift was known from its apparent and absolute rest-frame magnitude, the redshift dependence of this K-correction was not. In principle, this redshift dependence could have been calculated directly for each object using its best-fit spectrum returned from the photometric

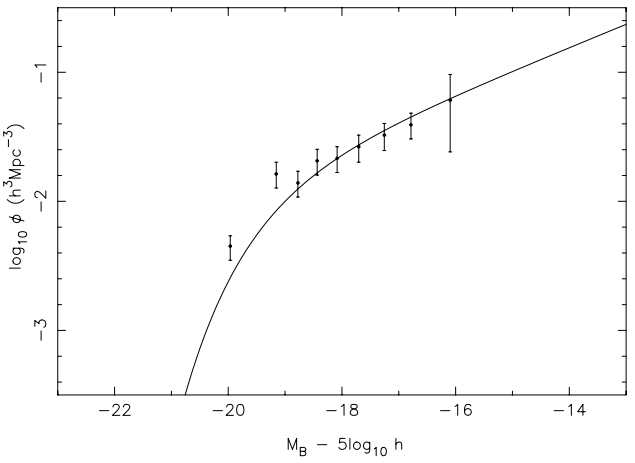

Figure 4. The CADIS B band object luminosity function calculated with the $1/V_{\rm max}$ formalism. Errors account only for errors in redshift. Points lie at bin centres, the widths of each chosen to hold the same number of objects. There are 371 galaxies in total selected by the redshift limits $0.3 \leq z \leq 0.8$ and the apparent B magnitude $m_{\rm B} \leq 24.5$. The solid line is the Schechter function determined in Section 4.2.

analysis. However, the much simplified approach of approximating the K-correction as a linear function of redshift was employed. This was primarily motivated by its improved efficiency and the relatively weak influence the K-correction was found to have on the final luminosity function. Lilly et al. (1995) find that the K-correction in their B-band for elliptical, spiral and irregular galaxies is proportional to redshift in the redshift range $0 \leq z \leq 0.8$. The following form for $K(z)$ was thus adopted

$$K(z) = \frac{K(z_0)}{z_0} z \tag{17}$$

where $K(z_0)$ is the K-correction of the object at its actual redshift z_0.

Once $V_{\rm max}$ has been calculated for all objects, the maximum likelihood estimated luminosity function ϕ at the rest-frame absolute magnitude M in bins of width $\mathrm{d}M$ is then,

$$\phi(M)\mathrm{d}M = \sum_i \frac{1}{V_{{\rm max},i}} \tag{18}$$

where the sum acts over all objects with magnitudes between $M - \mathrm{d}M/2$ and $M + \mathrm{d}M/2$.

Figure 4 shows the luminosity function of B band magnitudes from the CADIS offset field which has a solid viewing angle of $\delta\omega = 100$ arcmin^2. To match the selection of objects lying behind A1689, only objects within the redshift range $0.3 \leq z \leq 0.8$ were chosen. A further restriction on the apparent B magnitude of $m_{\rm B} \leq 24.5$ was applied for completeness of the sample (see Section 5.1), yielding a total of 371 galaxies. The data points in Figure 4 are centred on bins chosen to maintain an equal number of objects in each.

The 1σ errors shown here were calculated from Monte Carlo simulations. Object redshifts were randomly scattered in accordance with their associated errors provided in the CADIS dataset. For each realisation, the $V_{\rm max}$ of each object was re-calculated using the re-sampled redshift. The resulting standard deviation of the distribution of values of ϕ for each bin given by equation (18) was then taken as the error. In this particular instance, no consideration was given to the magnitude errors or the propagation of the redshift error into object magnitudes. Section 4.2 discusses this further.

4.2 Parameterisation of the CADIS B-band luminosity function

The maximum likelihood method of Sandage, Tammann & Yahil (1979, STY hereafter) was employed to determine the Schechter function best describing the CADIS B-band magnitudes. This parameterisation is essential for the determination of lens mass using the likelihood approach.

In much the same way as the probability in equation (1) was formed, the STY method forms the probability p_i that a galaxy i has an absolute magnitude M_i,

$$p_i \equiv p(M_i|z_i) \propto \frac{\phi(M_i)}{\int_{\max(M_{\min}(z_i),M_1)}^{\min(M_{\max}(z_i),M_2)} \phi(M)\mathrm{d}M} \tag{19}$$

where $M_{\rm max}(z_i)$ and $M_{\rm min}(z_i)$ are the absolute magnitude limits corresponding to the apparent magnitude limits of the survey at a redshift of z_i. Conversion of these apparent magnitude limits includes the K-correction using equation (16) with z set to z_i. A further restriction is placed upon the integration range by imposing another set of magnitude limits $M_1 < M < M_2$ which for the CADIS data were set at the maximum and minimum absolute magnitudes found in the sample.

The likelihood distribution in this case is a two dimensional function of the Schechter parameters M_* and α formed from the product of all probabilities p_i. The best fit M_* and α are therefore found by maximizing the likelihood function,

$$\begin{aligned} &\ln \mathcal{L}(M_*, \alpha) = \\ &\sum_{i=1}^{N} \left\{ \ln \phi(M_i) - \ln \textstyle\int_{\max(M_{\min}(z_i),M_1)}^{\min(M_{\max}(z_i),M_2)} \phi \,\mathrm{d}M \right\} + c_p \end{aligned} \tag{20}$$

with the constant c_p arising from the proportionality in equation (19). An estimate of the errors on M_* and α are calculated by finding the contour in α, M_* space which encompasses values of α and M_* lying within a desired confidence level about the maximum likelihood $\mathcal{L}_{\rm max}$.

To account for uncertainties in the Schechter parameters due to the redshift and magnitude errors derived by the photometric analysis, Monte Carlo simulations were once again performed. Redshifts and absolute magnitudes of the entire sample were randomly scattered before re-application of the maximum likelihood process each time. The error in absolute magnitude was calculated using simple error propagation through equation (16) yielding,

$$\sigma_{M_i}^2 = \left(\frac{K_i}{z_i} - \frac{5}{\ln 10} \frac{1 - 0.5(1+z_i)^{-1/2}}{1 + z_i - (1+z_i)^{1/2}} \right)^2 \sigma_{z_i}^2 + \sigma_{m_i}^2 \tag{21}$$

for each object with redshift z_i and apparent magnitude m_i. Here, the K-correction given by equation (17) has been used such that the quantity $K_i \equiv K(z_i)$ is calculated from equation (16) using m_i, M_i and z_i as they appeared in the CADIS

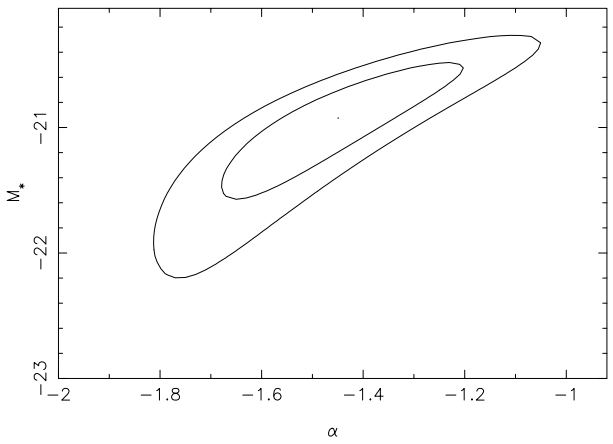

Figure 5. Likelihood contours for the CADIS B-band Schechter parameters taking photometric redshift and magnitude error into consideration. 1σ and 2σ confidence levels are plotted corresponding to $\Delta \ln \mathcal{L} = 1.15$ and 3.09 respectively.

dataset. The typical ratio of apparent magnitude to redshift error was found to be $\sigma_{m_i}/\sigma_{z_i} \sim 1\%$ due to the relatively imprecise nature of photometric redshift determination.

The final errors on M_* and α were taken from an effectively convolved likelihood distribution obtained by combining the scattered distributions produced from the Monte Carlo simulations. Figure 5 shows the final 1σ and 2σ likelihood contours calculated allowing for redshift and magnitude errors. These predict the resulting parameters

$$M_* = -19.43^{+0.47}_{-0.64} + 5\log_{10} h\,, \quad \alpha = -1.45^{+0.25}_{-0.23} \tag{22}$$

where projected 1σ errors are quoted. For completeness, the normalisation was also calculated to be

$$\phi^* = 0.0164\, h^3\, \mathrm{Mpc}^{-3}, \tag{23}$$

in this case where evolution of the luminosity function has been neglected.

5 SAMPLE CONSISTENCY

Ensuring that the A1689 sample of sources is consistent with the CADIS offset field sample is necessary to prevent biases from entering our results. The first level of compatibility we have already enforced by applying a redshift selection of $0.3 \leq z \leq 0.8$ to both samples. The second, discussed in Section 5.1 below, is sample completeness. A slightly less obvious consideration must also be given to galaxy morphological type as Section 5.2 explains.

5.1 Completeness

Determination of the faint magnitude limit beyond which both the A1689 and CADIS data set become incomplete is important for the calculation of an accurate lens mass. Both samples must be complete for fair comparison. Incorrect evaluation of the CADIS limiting magnitude results in larger values of $V_{\max}$ and hence a biased luminosity function not representative of the intrinsic A1689 distribution. Similarly, completeness of the A1689 sample also affects the lens mass in a manner quantified in Section 6.5.

Estimation of the completeness of both data sets was provided using the $V/V_{\max}$ statistic (Schmidt 1968). In this ratio, $V_{\max}$ is calculated using equation (14) whereas V is the comoving volume described by the observer's field of view from the same lower redshift limit in the integral of equation (14) to the redshift of the object. If a sample of objects is unclustered, exhibits no evolution and is complete, the position of each object in its associated volume $V_{\max}$ will be completely random. In this case, the distribution of the $V/V_{\max}$ statistic over the range 0 to 1 will be uniform with $\langle V/V_{\max}\rangle = 0.5$.

If the sample is affected by evolution such that more intrinsically bright objects lie at the outer edges of the $V_{\max}$ volume, then $V/V_{\max}$ is biased towards values larger than 0.5. The reverse is true if a larger number of brighter objects lie nearby. If the sample is incomplete at the limiting apparent magnitude chosen, estimations of $V_{\max}$ will be on average too large and will cause $V/V_{\max}$ to be biased towards values less than 0.5. The requirement that $\langle V/V_{\max}\rangle = 0.5$ for completeness is also subject to fluctuations due to finite numbers of objects. In the absence of clustering, the uncertainty due to shot noise on $\langle V/V_{\max}\rangle$ calculated from N galaxies can be simply shown to be

$$\sigma^2_{\langle V/V_{\max}\rangle} = \frac{1}{12N}. \tag{24}$$

In order to arrive at an apparent magnitude limit for the CADIS and A1689 fields, values of $\langle V/V_{\max}\rangle$ were calculated for different applied limiting magnitudes and plotted as shown in Figure 6. The grey region in this plot corresponds to the 1σ errors described by equation (24) which lessen at the fainter limiting magnitudes due to the inclusion of more objects. Clustering adds extra noise and so these errors are an underestimate of the true uncertainty (one can show that the uncertainty in $V/V_{\max}$ increases by the square root of the average number of objects per cluster).

Without knowledge of the effects of clustering, Figure 6 shows that a limiting magnitude of $m_{\rm B} \leq 24.5$ for CADIS and $m_{\rm B} \leq 23.6$ for A1689 corresponds to a value of $\langle V/V_{\max}\rangle \simeq 0.5$ and thus completeness. These magnitudes are in agreement with the apparent magnitude limits at which the number counts begin to fall beneath that measured by deeper surveys (such as the B band observations of Lilly, Cowie & Gardner (1991) which extend to a depth of $m_{\rm B} \simeq 26$) and also correspond to a 10σ object detection threshold deduced from the photometry.

Figure 7 shows the distribution of galaxies in the redshift–apparent magnitude plane in the Abell 1689 field. Abell 1689 itself can clearly been seen at $z = 0.18$. Superimposed is the region of parameter space we use for the mass determination with $0.3 < z < 0.8$ and $18 \leq m_{\rm B} \leq 23.6$ yielding 146 galaxies.

5.2 Morphological Type

Perhaps the most difficult inconsistency to quantify is that of variation in galaxy morphological type between samples. It has been known for some time that elliptical galaxies cluster more strongly than spirals (Davis & Geller 1976) and that

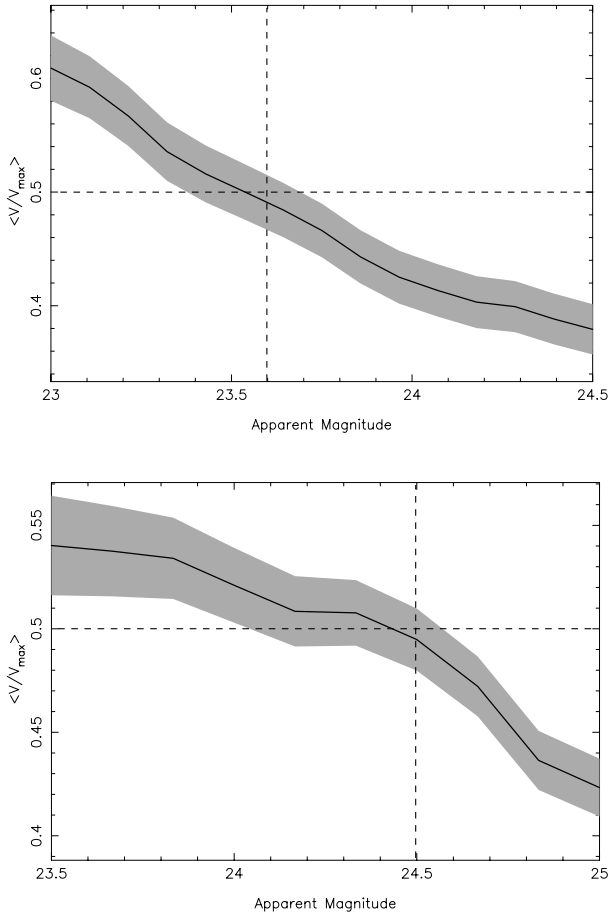

Figure 6. Variation of $V/V_{\rm max}$ with limiting apparent B magnitude for the A1689 (top) and the CADIS (bottom) sample. The grey region corresponds to the 1σ errors described by equation (24) which are an underestimate due to the unconsidered effects of galaxy clustering.

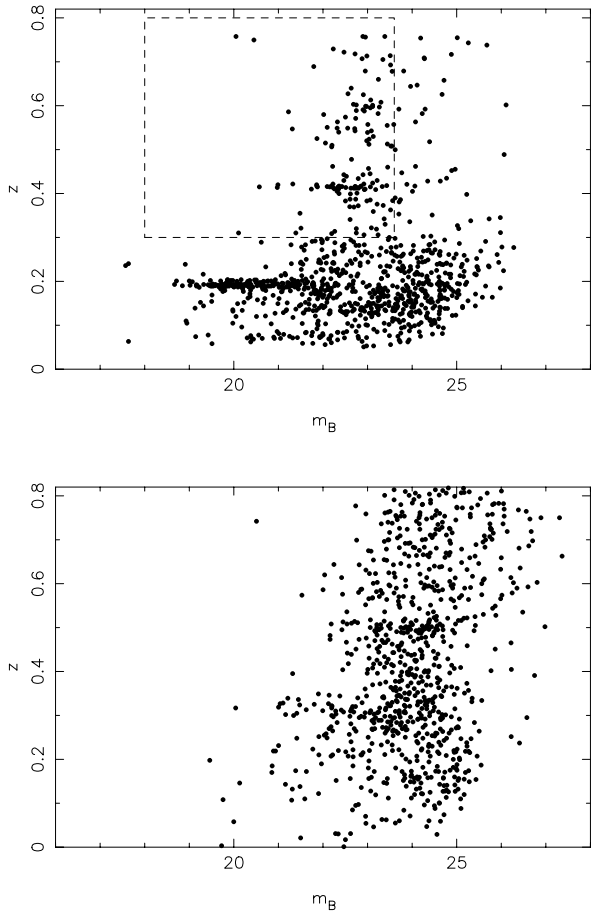

Figure 7. The Abell 1689 (top) and CADIS $16^{\rm h}$ (bottom) field redshift–apparent B magnitude parameter space. The dashed box highlights the selection criteria for the 146 A1689 background galaxies.

the elliptical fraction in clusters is an increasing function of local density (Dressler 1980). One might therefore expect a sample of galaxies lying behind a large cluster such as A1689 to contain a higher proportion of ellipticals than a sample of field galaxies away from a cluster environment. Since the luminosity function of E/S0 galaxies is thought to be different from that of spirals (see, for example, Chiba & Yoshii 1999 and references therein), comparison of our A1689 sample with the CADIS offset field sample may be expected to introduce a bias.

A related issue stems from the fact that the determination of an object's photometric redshift requires its detection in every filter belonging to the filter set. Both the CADIS and A1689 filter sets contain narrow band filters which cause the main restriction on which objects enter into the photometric analysis. Our $V/V_{\rm max}$ test in the B-band therefore does not give a true limiting B magnitude but one which applies only to objects detectable across all filters. As long as both samples under comparison are complete according to this test, the sole consequence of this is that certain morphological types will be under-represented. With the CADIS filter set of 16 filters differing from the 9 filters used for the observation of A1689, this again might be expected to cause inconsistent galaxy types between fields, biasing results.

Fortunately, our photometric analysis yields morphological type in addition to redshift. We are therefore able to directly measure the fraction of galaxies of a given type in both samples and thus test for biases. We find that in the CADIS sample, the ratio of E/S0:Spiral galaxies is $12\%\pm7\%$ and for the A1689 sample, this is $25\% \pm 13\%$ with Poisson errors quoted. This is in reasonable agreement with the canonical Postman and Geller (1984) E/S0:S fraction for field galaxies of about 30%. Approximately $60\% - 70\%$ of both samples are classified as starburst galaxies. Given the uncertainty in these fractions, we would argue that as far as we can tell, they are consistent with each other. Without a bigger sample of galaxies and possibly spectroscopically confirmed morphologies we are unable to do better although as the measurements stand, we would not expect any serious inconsistencies in morphology which would bias our results.

6 MASS DETERMINATION

Taking the CADIS luminosity function as a good estimate of the intrinsic distribution of A1689 source magnitudes in the range $0.3 \leq z \leq 0.8$, we can calculate κ_∞ and Σ assuming a relation between κ and γ. As noted in Section 4, in the absence of a detection of evolution of the luminosity function with redshift, we assume a no-evolution model for the background sources in this field. In general, the occurrence of evolution is anticipated however we expect its inclusion in the background model to have only a minor effect on the derived mass.

For the purpose of comparison with other studies we shall quote values of κ as well as κ_∞ and Σ. As κ is dependent on the source redshift, this is not a useful quantity to quote when the redshift distribution is known. The convergence we quote is the redshift averaged quantity defined by

$$\kappa = \frac{\kappa_\infty}{N_b} \sum_{i=1}^{N_b} f(z_i) = \kappa_\infty \langle f_b \rangle \tag{25}$$

where N_b is the number of source galaxies. For the field of Abell 1689 we find that $\langle f_b \rangle = 0.57$, giving an effective source redshift of $z_{\rm eff} = 0.45$.

6.1 Sources of uncertainty

Three sources of error on κ_∞ were taken into consideration:

1) The maximum likelihood error obtained from the width of the likelihood distribution at $\ln \mathcal{L}_{\rm max} - 0.5\Delta\chi^2$, with $\Delta\chi^2$ the desired confidence level. All object magnitudes and redshifts were taken as presented directly in the A1689 data while assuming the Schechter parameters from equation (22).
2) The uncertainty of the Schechter parameters M_* and α from the likelihood analysis of the CADIS offset field.
3) The redshift and magnitude uncertainties of individual objects in the A1689 data, derived from the photometric analysis.

In Section 7 we will show that the contribution of each source of uncertainty to the overall error depends on the number of galaxies included in the analysis. Taking all 146 galaxies across the entire field of view, the errors from each contributor listed above, expressed as a percentage of the total standard deviation were found to be; 50% from the maximum likelihood (essentially the shot noise), 25% from the uncertainty in M_* and α and 25% from the redshift and magnitude error.

The latter two sources of error in the above list were simultaneously included using the Monte Carlo method. 1000 simulations were carried out, randomly drawing values of M_* and α from the convolved likelihood distribution shown in Figure 5. For each realisation, redshifts and absolute magnitudes of objects in the A1689 field were scattered in exactly the same fashion as before with the CADIS dataset using their associated photometric errors. The standard deviation of the scattered values of κ_∞ produced in this way was then added in quadrature to the uncertainty of the maximum likelihood error obtained from item one of the list above to give the overall error.

The magnitude calibration error of $\sigma_{\Delta M} = 0.01$ discussed in Section 3.3 was ignored. Inspection of the form of the Schechter function in equation (3) shows that a systematic magnitude offset is exactly equivalent to an error in M_*. Clearly, the 1σ error quoted for M_* in equation (22) completely overwhelms this magnitude calibration uncertainty which was therefore deemed insignificant.

Finally, the dependence of our measurement of κ_∞ on the feature seen in the A1689 redshift distribution at $z \simeq 0.4$ was tested. We removed all galaxies contributing to this peak and re-calculated the results of the following two sections. Apart from a larger uncertainty due to the decreased number of objects, we found very little difference from the results obtained from the full dataset, indicating that our measurement is not dominated by the concentration of galaxies at $z \simeq 0.4$.

6.2 The differential radial κ profile

Background source objects from the A1689 data set were binned in concentric annuli about the cluster centre for the calculation of a radial mass profile. The relatively small number of objects contained in the sample however was unfortunately insufficient to allow computation of a profile similar in resolution to that of T98.

Apart from the effects of shot noise, this limitation results from the simple fact that bins which are too narrow do not typically contain a large enough number of intrinsically bright objects. This has the effect that the knee of the Schechter function assumed in the likelihood analysis is poorly constrained. As equation (1) shows, a large uncertainty in M_* directly results in a large error on the magnification and hence on κ_∞. Experimentation with a range of bin widths quickly showed that in order to achieve a tolerable precision for κ_∞, bins had to be at least ~ 1.1 arcmin in width. With the observed field of view, this gave a limiting number of three bins, illustrated spatially in the lower half of Figure 8. In Section 6.3 we find the average profile within an aperture, which provides a more robust measurement of κ.

The top half of Figure 8 shows the κ data points. These were converted from the maximum likelihood derived κ_∞ for each bin using equation (25). The profile of T98 is shown superimposed for comparison. Upper points correspond to the sheet estimator while the lower points are due to the isothermal estimator. The 1σ error bars plotted were calculated taking all three contributions listed in Section 6.1 into account.

Despite relatively large errors, the data points show an amplitude in good agreement with the profile derived from the number count study of T98. These errors seem large in comparison to those of the number count profile but the number count errors do not take the systematic uncertainties in background count normalisation, number count slope or background source redshift into consideration.

It is noticeable that the data points suggest a profile that is perhaps a little flatter than that derived by T98. It appears that more mass is detected at larger radii although this is not particularly significant.

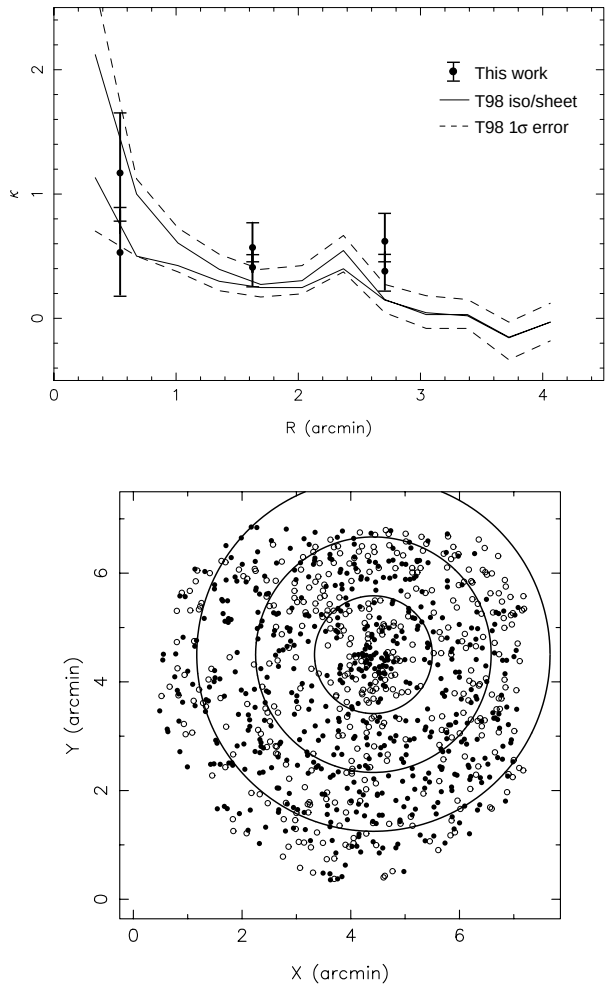

Figure 8. *Top* Comparison of radial κ profiles for A1689. Data points show isothermal (lower) and sheet (upper) estimated κ obtained from this work. 1σ error bars are plotted. The solid lines indicate the same isothermal/sheet estimator-bound profile obtained by T98 using integrated number counts with 1σ errors shown by dashed lines. *Bottom*: Spatial location of the annular bins on the A1689 field of view. Open dots are objects selected by $z > 0.2$ and solid dots by $z \leq 0.2$.

6.3 Aperture κ profile

In addition to the radial profile, the variation of average surface mass density contained within a given radius can be calculated. By applying the likelihood analysis to the objects contained within an aperture of varying size, a larger signal to noise can be attained at larger radii where more objects are encompassed. With a small aperture, the same low galaxy count problem is encountered as Figure 9 shows by the large uncertainty in this vicinity. In this plot, the parabolic estimator of equation (6) is used to obtain κ_∞ since as T98 show, this is a good average of the isothermal and sheet estimators and agrees well their self-consistent axi-symmetric solution. Application of the axi-symmetric solution is not viable in this case since we are limited to only 3 bins.

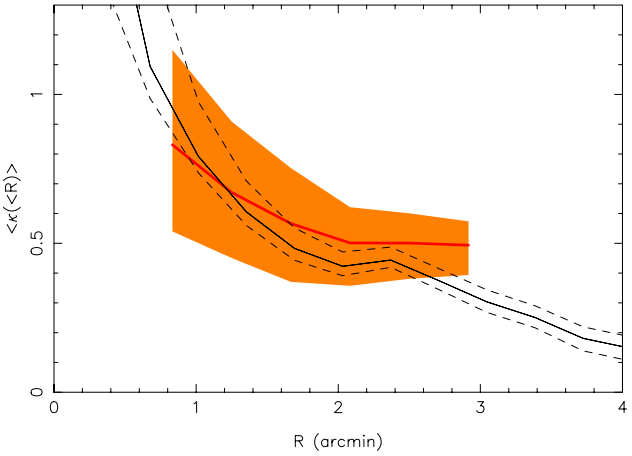

Figure 9. Variation of average surface mass density contained within a given radius R (thick dark line). 1σ errors are shown by the grey shaded region. The thin black solid and dashed lines show the average surface mass density and 1σ errors (due to likelihood analysis only) of the parabolic estimated profile of T98.

Radius (arcsec)	$M_{2d}(< R)$
65	$(0.16 \pm 0.09) \times 10^{15} h^{-1} \mathrm{M}_\odot$
130	$(0.48 \pm 0.16) \times 10^{15} h^{-1} \mathrm{M}_\odot$
195	$(1.03 \pm 0.27) \times 10^{15} h^{-1} \mathrm{M}_\odot$

Table 2. Cumulative projected mass given by the profile of Section 6.2.

Using equation (25), κ_∞ is again scaled to κ. The grey shaded region in Figure 9 depicts the 1σ errors, with the sources of uncertainty from Section 6.1 taken into account. The thin solid and dashed black lines show the variation of aperture κ and its error calculated by averaging the parabolic estimator profile presented in T98. The error does not account for uncertainties arising from background count normalisation, number count slope or background source redshift. The results of T98 were shown to be in good agreement with the shear analysis of Kaiser (1996) and hence we find a consistent picture of the mass amplitude and slope from all three independent methods.

As expected from the results of Section 6.2, generally more mass than that predicted from the number counts is seen, especially at large radii. The following section quantifies this for a comparison with the projected mass result of T98.

6.4 Projected mass

From the values of κ_∞ used to generate the κ profile in Section 6.2 and the result of equation (5), the cumulative projected masses in Table 2 were calculated. Errors were derived from propagation of the errors on the binned values of κ_∞.

These projected masses are in excellent agreement

$m_{\max}$	M_*	α	κ_∞(iso)	κ_∞(para)	κ_∞(sheet)
25.5	−19.06	−0.80	$0.61^{+0.03}_{-0.04}$	$0.69^{+0.04}_{-0.06}$	$0.76^{+0.07}_{-0.08}$
25.0	−19.25	−1.10	$0.65^{+0.04}_{-0.04}$	$0.77^{+0.06}_{-0.06}$	$0.84^{+0.08}_{-0.09}$
24.5	−19.43	−1.45	$0.70^{+0.06}_{-0.04}$	$0.85^{+0.08}_{-0.08}$	$0.96^{+0.10}_{-0.10}$
24.0	−19.98	−1.87	$0.74^{+0.03}_{-0.04}$	$0.91^{+0.13}_{-0.12}$	$1.08^{+0.16}_{-0.17}$
23.5	−19.24	−1.53	$0.75^{+0.04}_{-0.04}$	$0.90^{+0.06}_{-0.07}$	$1.10^{+0.10}_{-0.09}$

Table 3. Variation of limiting apparent B magnitude $m_{\max}$ of the CADIS field and its effect on the Schechter parameters and the resulting value of κ_∞. Values of M_* assume $h = 1$. The apparent magnitude limit of $b = 23.6$ was assumed for the A1689 data in calculating the maximum likelihood κ_∞. Errors here are taken only from the width of the likelihood curves.

with those of T98. At the redshift of the cluster $1' = 0.117\,h^{-1}$ Mpc and hence the second cumulative mass listed in Table 2 gives

$$M_{2d}(< 0.25\,h^{-1}\,\mathrm{Mpc}) = (0.48 \pm 0.16) \times 10^{15}\,h^{-1}\mathrm{M}_\odot \quad (26)$$

which is perfectly consistent with the result from the number count study. The error here is comparable to the 30% error quoted for the result of T98 when allowing for all sources of uncertainty. The projected mass contained within 195 arcsec is a little higher than that predicted by T98 although remains arguably consistent given the errors involved in each.

6.5 Effects of sample incompleteness

One final uncertainty not taken into consideration so far is that of sample incompleteness. Changing the limiting apparent B magnitude in the determination of the CADIS luminosity function directly affects the fitted values of M_*, α and hence the maximum likelihood κ_∞. Similarly, differing numbers of objects included in the A1689 sample from variations in its limiting magnitude also has an influence on κ_∞.

Table 3 quantifies this effect for the CADIS objects. It can be seen that increasing the faint limit $m_{\max}$ (ie. including fainter objects) has little effect on κ_∞ until the limit $m_{\max} \simeq 24.5$ is reached. Beyond this limit, κ_∞ starts to fall. Two inferences can therefore be made. Firstly, this suggests that the magnitude limit in Section 5.1 from the $V/V_{\max}$ test, being consistent with the limit here, was correctly chosen. Secondly, κ_∞ is relatively insensitive to the choice of $m_{\max}$ if the sample is complete (and not smaller than the limit at which shot noise starts to take effect).

The effect of varying the magnitude limit of the A1689 sample is quantified in Table 4. A clear trend is also seen here; as its limiting faint magnitude $m_{\max}$ is reduced, κ_∞ falls. Assuming linearity, a rough estimate of the uncertainty of κ_∞ given the uncertainty of the sample magnitude limit is given by:

$$\Delta\kappa_\infty = \begin{cases} \sim 0.1\Delta m_{\max} & \text{isothermal} \\ \sim 0.2\Delta m_{\max} & \text{parabolic} \\ \sim 0.4\Delta m_{\max} & \text{sheet} \end{cases} \quad (27)$$

Referring to Figure 6, a suitable uncertainty in $m_{\max}$ of the A1689 sample of say ± 0.2 magnitudes might be argued. If this were the case, the projected masses of the previous section calculated with the parabolic estimator would have a further error of $\sim 5\%$ which is negligibly small.

$m_{\max}$	κ_∞(iso)	κ_∞(para)	κ_∞(sheet)
24.5	$0.77^{+0.03}_{-0.03}$	$1.03^{+0.11}_{-0.11}$	$1.30^{+0.15}_{-0.13}$
24.0	$0.76^{+0.04}_{-0.04}$	$0.94^{+0.10}_{-0.10}$	$1.12^{+0.13}_{-0.12}$
23.5	$0.69^{+0.06}_{-0.07}$	$0.79^{+0.10}_{-0.11}$	$0.92^{+0.13}_{-0.12}$

Table 4. Variation of the maximum likelihood determined κ_∞ with limiting apparent B magnitude $m_{\max}$ of the A1689 data. The Schechter parameters of Section 4.2 were assumed in the likelihood analysis.

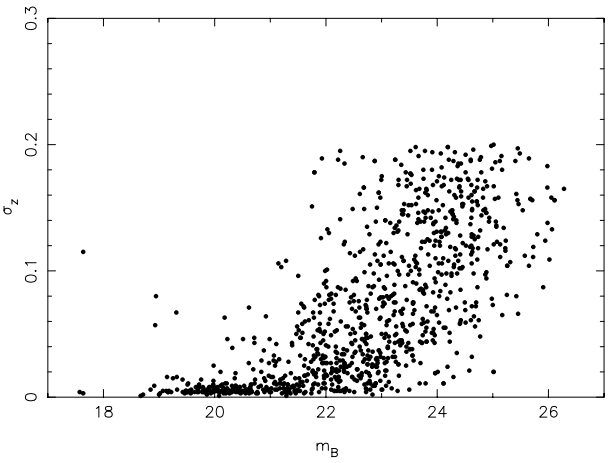

Figure 10. Correlation of photometric redshift error with apparent B-band magnitude for the A1689 data. No significant correlation between σ_z and z exists.

7 SIGNAL-TO-NOISE PREDICTIONS

Including all possible contributions of uncertainty in the calculation of mass, the previous section showed that even with relatively few galaxies, a significant cluster mass profile can be detected. One can make predictions of the sensitivity of the method with differing input parameters potentially obtained by future measurements. This exercise also serves as an optimisation study, enabling identification of quantities requiring more careful measurement and those which play an insignificant part.

The most convenient means of carrying out this investigation is by application of the reconstruction method to simulated galaxy catalogues. Catalogues were therefore constructed by randomly sampling absolute magnitudes from the Schechter function fitted to the CADIS offset field in Section 4.2. Redshifts were assigned to each magnitude by randomly sampling the distribution parameterised by T98 (their equation 22) from the Canada France Redshift Survey (Lilly et al. 1995). A range of catalogues were produced, varying by the number of objects they contained and their distribution of galaxy redshift errors modeled from the A1689 data.

Figure 10 shows how the distribution of photometric

redshift error, σ_z, correlates with the A1689 B-band apparent magnitude. No significant correlation between σ_z and redshift was found. Catalogue objects were thus randomly assigned redshift errors in accordance with their apparent magnitude, given by the correlated distribution in Figure 10. Different catalogues were generated from different scalings of this distribution along the σ_z axis.

Each catalogue was then lensed with a sheet mass characterised by $\kappa_\infty = 1$ before applying the reconstruction. 1000 Monte Carlo realisations were performed for each reconstruction, scattering object redshifts according to their assigned errors in the same manner as in the reconstruction of A1689. Furthermore, to model the uncertainty associated with the offset field, assumed values of the Schechter parameters M_* and α were once again subject to Monte Carlo realisations. All catalogues were reconstructed assuming sets of Schechter parameters drawn from a range of scaled versions of the distribution shown in Figure 5.

The resulting scatter measured in the reconstructed value of κ_∞ for each catalogue and assumed α-M_* scaling was combined with the average maximum likelihood error across all realisations of that catalogue to give an overall error. This total error was found to be well described by,

$$\sigma^2_{\kappa_\infty} = \frac{1+(2\sigma_z)^2}{n} + (0.12\sigma_{M_*})^2 + (0.37\sigma_\alpha)^2 - 0.18\sigma_{\alpha M_*} \quad (28)$$

where n is the number of galaxies, σ_z is the sample average redshift error and σ_{M_*} and σ_α are the projected errors on M_* and α respectively as quoted in equation (22). The quantity $\sigma_{\alpha M_*}$ is the covariance of α and M_* defined by

$$\sigma_{\alpha M_*} = \frac{\int \mathcal{L}(M_*,\alpha)(M_* - \langle M_*\rangle)(\alpha - \langle\alpha\rangle)\ \mathrm{d}M_*\mathrm{d}\alpha}{\int \mathcal{L}(M_*,\alpha)\ \mathrm{d}M_*\mathrm{d}\alpha} \quad (29)$$

where the likelihood distribution $\mathcal{L}$ is given by equation (20). We find that $\sigma_{\alpha M_*} = 0.039$ for the CADIS offset field. Equation (28) is valid for $n \geq 20$ and $0.0 \geq \sigma_z \geq 0.3$.

Equation (28) shows that when the number of objects is low, shot noise dominates. With $n \simeq 200$ however, uncertainties from the calibration of the offset field start to become dominant. The factor of 2 in the photometric redshift error term stems from the fact that redshift errors also translate directly into absolute magnitude errors through equation (21). Another discrepancy arises when comparing this redshift error with the redshift error contribution of 25% claimed for the A1689 data in Section 6.1. This is accounted for by the fact that K-corrections were present in the A1689 data whereas in the simulated catalogues there were not. Equation (21) quantifies the increase in magnitude error with the inclusion of K-corrections. This translates to an approximate increase of 20% in the overall error with an average K-correction of -1.0 for the A1689 data.

Emphasis should be placed on the criteria for which equation (28) is valid. The predicted overall error rises dramatically when fewer than $\simeq 20$ objects are included in the analysis. Simulations with 15 objects resulted in maximum likelihood errors rising to beyond twice that predicted by simple shot noise. This stems mainly from the effect mentioned in Section 6.2, namely the failure of the likelihood method when the knee of the Schechter function is poorly constrained.

The most immediate improvement to a multi-colour study such as this would therefore be to increase galaxy numbers. As previously noted, only when bins contain $\simeq 200$ objects do offset field uncertainties become important. Observing in broader filters is one way to combat the limit presented by galaxy numbers. Section 3.2 noted how the 3000 galaxies detected in the I band image were instantly reduced to 1000 by the shallow depth limit placed by the narrow 466/8 filter, even though both were observed to similar integration times. Using broader filters will also inevitably give rise to less accurate photometric redshifts. However as the analysis of this section has shown, one can afford to sacrifice redshift accuracy quite considerably before its contribution becomes comparable to that of shot noise.

Deeper observations provide another obvious means of increasing the number of galaxies. The error predictions above indicate that the expected increase in galaxy numbers using an 8 metre class telescope with the same exposure times as those in this work should reduce shot noise by a factor of ~ 3. Since deeper observations would also reduce redshift and offset field calibration uncertainties to negligible levels, the only source of error would be shot noise. In this case, the signal to noise for κ_∞ from equation (28) becomes simply $\kappa_\infty\sqrt{n}$ and hence our mass estimate for A1689 could be quoted with a 9σ certainty.

8 SUMMARY

Photometric redshifts and magnitudes have been determined for objects in the field of Abell 1689 from multi-waveband observations. This has allowed calculation of the luminosity function of source galaxies lying behind the cluster. Comparison of this with the luminosity function obtained from a similar selection of objects in an unlensed offset field has resulted in the detection of a bias in the A1689 background object magnitudes attributed to lens magnification by the cluster.

To ensure that systematic biases do not affect our results, we have given careful consideration to the consistency between both the A1689 dataset and the CADIS offset field dataset. We find the distribution of galaxy types within the redshift range $0.3 \leq z \leq 0.8$ applied to both samples to be very similar. This demonstrates that our lower redshift cutoff is sufficient to prevent objects in the A1689 dataset from being significantly influenced by the cluster environment.

After allowing for sources of uncertainty due to redshift and magnitude error, offset field calibration error and likelihood error (including shot noise), a significant radial mass profile for A1689 has been calculated. We predict a projected mass interior to $0.25\,h^{-1}$ Mpc of

$$M_{2d}(< 0.25\,h^{-1}\,\mathrm{Mpc}) = (0.48 \pm 0.16) \times 10^{15}\,h^{-1}\mathrm{M}_\odot \quad (30)$$

in excellent agreement with the number count analysis of T98 and the shear results of Tyson & Fischer (1995) and Kaiser (1995).

We can compare the efficiency of the method presented in this paper in terms of telescope time and signal-to-noise with the number count method used by T98. The 5.5σ result quoted by T98 does not include uncertainty due to their background count normalisation, number count slope or background source redshift distribution. Adding these errors to their result gives an estimated signal-to-noise of 3σ, the same as this work. Regarding telescope time, we define

a 'total information content' for each study as the product of telescope collecting area and total integration time. T98 observed 6000s in each of the V and I bands with the NTT 3.6m. Comparing with the CA 3.5m telescope and 12 hours integration time used in this study shows that we have amassed a total information content of approximately 3 times that required for the T98 result.

Despite the extra time penalty induced by our method, we note that deeper observations, especially in the narrow band filters used, would increase the signal-to-noise of our result significantly since we are dominated by shot noise. Our signal-to-noise analyses in Section 7 showed that a 9σ detection of mass would be possible using an 8 metre class telescope, equivalent to an increase in integration time by a factor of 5. This is in contrast to T98 whose main source of uncertainty comes from the unknown source redshift distribution. Shot-noise makes a negligible contribution to their error to the extent that increasing their total integration time by a factor of three to match the total information content of this work would still result in a signal-to-noise of 3σ (Dye 1999).

This paper has been primarily devoted to establishing the viability of lens mass reconstruction using the luminosity function method. We have shown that the two main advantages over the number count method employed by T98 are that use of photometric redshifts have enabled breaking of the mass/background degeneracy and that the technique is independent of their clustering if it is assumed that they form an effective random sampling of luminosity space.

ACKNOWLEDGEMENTS

SD thanks PPARC for a studentship and the IfA Edinburgh for funding, ANT thanks PPARC for a research fellowship and EMT thanks the Deutsche Forschungsgemeinschaft for the research fellowship supporting his stay in Edinburgh. We also thank Tom Broadhurst for use of his I-band data and Narciso Benitez who performed the original data reduction.

REFERENCES

Athreya R., Mellier Y., van Waerbeke L., Fort B., Pelló R. & Dantel-Fort M., 1999, submitted to A&A, astro-ph/9909518

Bertin E. & Arnouts S., 1996, A&AS, 117, 393

Broadhurst T.J., Taylor A.N. & Peacock J.A., 1995, ApJ, 438, 49

Chiba M. & Yoshii Y., 1999, ApJ, 510, 42

Davis M. & Geller M.J., 1976, ApJ, 208, 13

Dressler A., 1980, ApJ, 236, 351

Dye S., 1999, PhD Thesis, University of Edinburgh, UK

Ellis R.S., Colless M., Broadhurst T., Heyl J., Glazebrook K., 1996, MNRAS, 280, 235

Falco E.E., Gorenstein M.V. & Shapiro I.I., 1985, ApJ, 437, 56

Fort B., Mellier Y. & Dantel-Fort M., 1997, A&A, 321, 353

Francis P.J., Hewett P.C., Foltz C.B., Chaffee F.H., Weymann R.J., Morris S.L., 1991, ApJ, 373, 465

Gray M.E., Ellis R.E., Refregier A., Bézecourt J., McMahon R.G., Beckett M.G., Mackay C.D. & Hoenig M.D., 2000, submitted to MNRAS, astro-ph/0004161

Gunn J.E. & Stryker L.L., 1983, ApJS, 52, 121

Kaiser N., 1996, in O. Lahav, E. Terlevich, R.J. Terlevich, eds, Proc. Herstmonceux Conf. 36, Gravitational Dynamics, Cambridge University Press, p.181

Kinney A.L., Calzetti D., Bohlin R.C., McQuade K., Storchi-Bergmann T., Schmitt H.R., 1996, ApJ, 467, 38

Lilly S.J., Cowie L.L. & Gardner J.P., 1991, ApJ, 369, 79

Lilly S.J., Tresse L., Hammer F., Crampton D., Le Févre O., 1995 ApJ, 455, 108

Mayen C. & Soucail G., 2000, submitted to A&A, astro-ph/0003332

Meisenheimer K., Röser H.J., 1996, MPIAPHOT User Manual, MPIA Heidelberg

Meisenheimer K. et al., 1998, in S. D'Oderico, A.Fontana, E. Giallongo, eds, ASP Conf. Ser. Vol. 146, The Young Universe: Galaxy Formation and Evolution at Intermediate and High Redshift, p.134

Oke J.B., 1990, AJ, 99, 1621

Parzen E., 1963, Proc. Symp. on Time Series Analysis, p.155, ed. I.M. Rosenblatt

Pickles A.J. & van der Kruit P.C., 1991, A&AS, 91, 1

Postman M. & Geller M.J., 1984, ApJ, 281, 95

Rögnvaldsson Ö.E., Greve T.R., Hjorth J., Gudmundsson E.H., Sigmundsson V.S., Jakobsson P., Jaunsen A.O., Christensen L.L., van Kampen E. & Taylor A.N., 2000, submitted to MNRAS, astro-ph/0009045

Sandage A., Tammann G.A. & Yahil A., 1979, ApJ, 232, 352

Schmidt M., 1968, ApJ, 151, 393

Taylor A.N., Dye S., Broadhurst T.J., Benitez N., van Kampen E., 1998, ApJ, 501, 539

Teague P.F., Carter D. & Gray P.M., 1990, ApJS, 72, 715

Thommes E.M. et al., 1999, 'CADIS Revised Proposal', MPIA Publication

Tyson J.A. & Fischer P., 1995, ApJ, 446, L55

van Kampen E., 1998, MNRAS, 301, 389

Wolf C., Meisenheimer K., Röser H.J., Beckwith S., Fockenbrock H., Hippelein H., Phleps S., Thommes E., 1999, A&A, 343, 399